May 9, 2005

Aerosol properties computed from aircraft-based observations during the ACE-Asia campaign: 2. A case study of lidar ratio closure and aerosol radiative effects

Authors:
M. Kuzmanoski‡, M. A. Box, B. Schmid, G. P. Box, J. Wang, P. B. Russell, D. Bates, H. H. Jonsson, E. J. Welton*, R. C. Flagan, J. H. Seinfeld

Submission to: Journal of Geophysical Research - Atmospheres

For a vertical profile with three distinct layers (marine boundary, pollution and dust), observed during the ACE-Asia campaign, we carried out a comparison between the modeled lidar ratio vertical profile and that obtained from collocated airborne NASA AATS-14 sunphotometer and shipborne Micro-Pulse Lidar (MPL) measurements. Vertically resolved lidar ratio was calculated from two size distribution vertical profiles – one obtained by inversion of sunphotometer-derived extinction spectra, and one measured in-situ – combined with the same refractive index model based on aerosol chemical composition. The aerosol model implies single scattering albedos of 0.78 – 0.81 and 0.93 – 0.96 at 0.523 μm (the wavelength of the lidar measurements), in the pollution and dust layers, respectively. The lidar ratios calculated from the two size distribution profiles have close values in the dust layer; they are however, significantly lower than the lidar ratios derived from combined lidar and sunphotometer measurements, most probably due to the use of a simple nonspherical model with a single particle shape in our calculations. In the pollution layer, the two size distribution profiles yield generally different lidar ratios. The retrieved size distributions yield a lidar ratio which is in better agreement with that derived from lidar/sunphotometer measurements in this layer, with still large differences at certain altitudes (the largest relative difference was 46%). We explain these differences by non-uniqueness of the result of the size distribution retrieval and lack of information on vertical variability of particle refractive index. Radiative transfer calculations for this profile showed significant atmospheric radiative forcing, which occurred mainly in the pollution layer. We demonstrate that if the extinction profile is known then information on the vertical structure of absorption and asymmetry parameter is not significant for estimating forcing at TOA and the surface, while it is of importance for estimating vertical profiles of radiative forcing and heating rates.

‡ Lead Author: Maja Kuzmanoski
School of Physics, University of New South Wales
Sydney, Australia

* Co-Author: Dr. E. J. Welton
NASA GSFC Code 613.1
Ellsworth.J.Welton@nasa.gov

Aerosol properties computed from aircraft-based observations during the ACE-Asia campaign: 2. A case study of lidar ratio closure and aerosol radiative effects

M. Kuzmanoski[1], M. A. Box[1], B. Schmid[2], G. P. Box[1], J. Wang[3], P. B. Russell[4], D. Bates[5], H. H. Jonsson[6], E. J. Welton[7], R. C. Flagan[8], J. H. Seinfeld[8]

[1]School of Physics, University of New South Wales, Sydney, NSW 2052, Australia (e-mail: mkuzm@phys.unsw.edu.au, m.box@unsw.edu.au, gpb@newt.phys.unsw.edu.au)

[2] Bay Area Environmental Research Institute, 560 3rd Street West, Sonoma, CA 95476. (e-mail: bschmid@mail.arc.nasa.gov)

[3]Brookhaven National Laboratory, Upton, NY, 11973 (e-mail: jian@bnl.gov)

[4] NASA Ames Research Center, MS 245-5, Moffett Field, CA 94035-1000. (e-mail: Philip.B.Russell@nasa.gov)

[5] Physics Department, University of Miami, 1320 Campo Sano Drive, Coral Gables, FL 33146. (e-mail: bates@physics.miami.edu)

[6] CIRPAS, 3200 Imjin Road, Marina, CA 93933. (e-mail: hjonsson@nps.navy.mil)

[7] NASA Goddard Space Flight Center, Laboratory for Atmospheres, Code 912, Greenbelt, MD 20771. (e-mail: Ellsworth.J.Welton@nasa.gov)

[8]Department of Chemical Engineering, California Institute of Technology, Pasadena, California (email: flagan@cheme.caltech.edu, seinfeld@caltech.edu)

Abstract. For a vertical profile with three distinct layers (marine boundary, pollution and dust), observed during the ACE-Asia campaign, we carried out a comparison between the modeled lidar ratio vertical profile and that obtained from collocated airborne NASA AATS-14 sunphotometer and shipborne Micro-Pulse Lidar (MPL) measurements. Vertically resolved lidar ratio was calculated from two size distribution vertical profiles – one obtained by inversion of sunphotometer-derived extinction spectra, and one measured in-situ – combined with the same refractive index model based on aerosol chemical composition. The aerosol model implies single scattering albedos of 0.78 – 0.81 and 0.93 – 0.96 at 0.523 μm (the wavelength of the lidar measurements), in the pollution and dust layers, respectively. The lidar ratios calculated from the two size distribution profiles have close values in the dust layer; they are however, significantly lower than the lidar ratios derived from combined lidar and sunphotometer measurements, most probably due to the use of a simple nonspherical model with a single particle shape in our calculations. In the pollution layer, the two size distribution profiles yield generally different lidar ratios. The retrieved size distributions yield a lidar ratio which is in better agreement with that derived from lidar/sunphotometer measurements in this layer, with still large differences at certain altitudes (the largest relative difference was 46%). We explain these differences by non-uniqueness of the result of the size distribution retrieval and lack of information on vertical variability of particle refractive index. Radiative transfer calculations for this profile showed significant atmospheric radiative forcing, which occurred mainly in the pollution layer. We demonstrate that if the extinction profile is known then information on the vertical structure of absorption and asymmetry parameter is not significant for estimating forcing at TOA and the surface, while it is of importance for estimating vertical profiles of radiative forcing and heating rates.

1. Introduction

Radiative forcing caused by aerosols is one of the major uncertainties in estimating the Earth's radiation budget [*Intergovernmental Panel on Climate Change (IPCC)*, 2001]. The impact of aerosol on climate is controlled by their optical properties, such as optical thickness, single scattering albedo and asymmetry parameter. These quantities can be derived from measurements, or evaluated from the available information on aerosol size distribution, shape, chemical composition and mixing state. Comparative studies of different measurement methods, as well as measured and modeled aerosol optical properties, are useful in efforts to improve our understanding of the role of aerosols in radiative transfer. Such studies are referred to as closure studies, and are one of major focuses of the ACE-Asia campaign [*Huebert et al.*, 2003] and previous aerosol characterization experiments, such as ACE 1 [*Bates et al.*, 1998], ACE 2 [*Russell and Heintzenberg*, 2000], TARFOX [*Russell et al.*, 1999], LACE98 [*Ansmann et al.*, 2002].

Lidar ratio, or extinction-to-backscatter ratio, is an essential parameter in analyzing lidar signals. While independent measurements of extinction and backscattering coefficient vertical profiles can be obtained by Raman lidar [*Melfi*, 1972; *Ansmann et al.*, 1990; 1992] and high-spectral-resolution lidar [*Shipley et al.*, 1983], obtaining the extinction coefficient from the elastic backscatter lidar measurements requires a priori knowledge of the lidar ratio. This property can be obtained by combining backscatter lidar measurements with information on layer optical thickness, derived from coincident radiometer or sunphotometer measurements [*Welton et al.*, 2000] or from slant-path lidar measurements [*Spinhirne et al.*, 1980; *Powell et al.*, 2000]. *Schmid et al.* [2003] combined airborne sunphotometer and shipborne lidar measurements to derive the vertical profile of the lidar ratio needed to yield exact agreement between the lidar-derived and sunphotometer-derived vertical profiles of aerosol extinction.

Lidar ratio can also be estimated from aerosol size distributions (measured in-situ, or retrieved from aerosol optical properties) and a suitable refractive index model.

In the present work, comparison of modeled vertical profile of lidar ratio, with the one derived by *Schmid et al.* [2003] from coincident airborne sunphotometer and shipborne lidar measurements (the implied lidar ratio), is carried out. Previous studies on comparisons of lidar measurements with calculations from in-situ measured size distributions concentrated mainly on minimizing the differences between the modeled and measured extinction and backscattering, in order to find the real part of the refractive index and the single scattering albedo [*Redemann et al.*, 1998, 2000a; *Ferrare et al.*, 1998], or used information on aerosol chemical composition in order to derive the mixing state [*Fiebig et al.*, 2002]. Some studies focused on comparison of directly measured lidar ratio and that derived from aerosol size distributions, using Mie theory [*Liu et al.*, 2002; *Masonis et al.*, 2003]. Lidar ratio can also be predicted from the information on wavelength dependence of aerosol extinction, using aerosol size distribution retrieval as an intermediate step. *Rajeev and Parameswaran* [1998] employed the size distribution retrieval method of *King et al.* [1978] in an iterative algorithm for analyzing multi-wavelength lidar signal to obtain vertical profiles of aerosol extinction spectra and size distributions. However, the approach discussed here, which involves size distribution retrieval, was not used before as a means of comparing airborne sunphotometer with lidar measurements.

Focusing on the profile observed on April 17, 2001 as part of the ACE-Asia campaign, and studied in Part I for aerosol size distributions, we compare lidar ratios calculated from two size distribution profiles – one retrieved from sunphotometer-derived extinction, and one measured in-situ – in three distinct layers observed on this day. The refractive index used is based on the analysis of aerosol chemical composition. Modeled lidar ratios are compared with the one derived from collocated airborne sunphotometer and shipbased backscatter lidar

measurements. In addition, the aerosol model based on retrieved aerosol size distributions was used to estimate the aerosol radiative effects. Due to the high sensitivity of the lidar ratio to particle size distribution and both the real and imaginary parts of the particle refractive index, comparison of its modeled and measured values is convenient for testing the validity of the aerosol model for use in estimating the aerosol radiative forcing.

2. Measurements

Measurements relevant for this work were carried out aboard the CIRPAS Twin Otter aircraft [*Bane et al.*, 2004]. The details about aerosol optical depth and size distribution measurements are given by *Schmid et al.* [2003] and *Wang et al.* [2002], respectively. In brief, aerosol optical depth was measured at 13 wavelengths, in the wavelength range from 0.354 μm to 1.558 μm, using a 14-channel NASA Ames Airborne Suntracking Sunphotometer (AATS-14). *Schmid et al.* [2003] differentiated aerosol optical depths measured in vertical profile to obtain aerosol extinction. In the present work, the aerosol extinction spectra are used for retrieval of vertical profile of aerosol size distribution. The size distribution measurements were carried out in the particle diameter range of 0.15 μm – 10 μm, using a combination of an Aerodynamic Particle Sizer (APS) and a Differential Mobility Analyzer (DMA) System [*Wang et al.*, 2002].

For aerosol chemical composition measurements, 8 MOUDI and 3 denuder samplers operated aboard the Twin Otter aircraft [*Wang et al.*, 2002]. Although each MOUDI had 5 stages, only one of them (collecting particles with diameters up to 3 μm) was in operation. The collected samples were analyzed for metallic elements, and water-soluble anionic species, while the denuder samplers were used for analyzing OC and EC. The Tandem DMA was used for measurement of aerosol hygroscopic properties.

The Micro-Pulse Lidar (MPL) [*Spinhirne et al.*, 1995] is a single channel lidar, operating at wavelength 0.523 μm. During the ACE-Asia campaign, it performed measurements aboard the NOAA ship R/V Ronald H. Brown, and its signal was analyzed for vertical profiles of extinction and backscattering coefficients. Analysis of the MPL signal requires knowledge of the extinction-to-backscatter ratio (lidar ratio). In a standard procedure followed by the MPLNET [*Welton et al.*, 2001], a network of MPLs collocated with the AERONET Sun/sky radiometers [*Holben et al.*, 1998], the extinction profile derived from the lidar measurements is constrained by the Sun/sky radiometer-measured aerosol optical depth.

3. Lidar ratio

Three Twin Otter vertical profiles during the ACE-Asia campaign coincided with the lidar measurements aboard the R/V Ronald H. Brown. Assuming that the lidar ratio had a constant value at all altitudes of the profile flown by the Twin Otter, and another value above the top of the profile, the lidar signal retrieval for these cases was constrained by the sunphotometer-measured optical thickness values at $\lambda = 0.525$ μm, for the total column and at the top of the profile [*Schmid et al.*, 2003]. As they pointed out, this is different from the MPLNET standard procedure. For two cases they calculated the vertically resolved lidar ratio, required for the agreement of the lidar-derived extinction profile with that derived from the sunphotometer measurements at 0.525 μm (the implied lidar ratio). Here we calculate the vertical profile of the lidar ratio, using both the in-situ measured size distributions and those retrieved from the sunphotometer measurements. We concentrate on the April 17, 2001 profile, since for this case the aerosol refractive index values were derived from the airborne chemical measurements. On this day, the aircraft flew a vertical profile from 0.09 to 3.43 km. The left panel of Figure 1 shows the extinction profile derived by *Schmid et al.* [2003] from the

sunphotometer measurements, and boundaries between three distinct layers observed: marine boundary, pollution and free tropospheric (dust) layer, all with different particle physical and chemical characteristics.

The formula used in this paper for calculation of the lidar ratio is:

$$S = \frac{4\pi}{\omega_0 \cdot p(180^\circ)}. \quad (1)$$

Here, ω_0 is the single scattering albedo, and $p(180^\circ)$ is the phase function in the backscattering direction, with normalization:

$$\frac{1}{2}\int_0^\pi p(\theta)\sin\theta d\theta = 1. \quad (2)$$

3.1. Aerosol model

As noted previously, we obtained the size distribution vertical profiles from the in-situ measurements, using DMA and APS, and by inversion of sunphotometer-derived extinction spectra. The size distribution retrievals were carried out with a vertical resolution of ~ 40 – 50 *m*, using the constrained linear inversion method [*King et al.*, 1978]. Both the retrieved and measured size distribution profiles, coupled with the size-resolved refractive index based on aerosol chemical composition measured in each layer (calculated by *Wang et al.* [2002]), were used for calculating the single scattering albedo and backscattering phase function. Calculating the refractive index values for each of the layers observed in the profile, *Wang et al.* [2002] assumed that aerosols were internal mixtures of different species, and used the ISORROPIA thermodynamic equilibrium model [*Nenes et al.*, 1998] and Bruggeman mixing rule. They justified the assumption of an internal mixture by the results of the Tandem DMA measurements, which revealed that particles of the same dry size grew to similar sizes at high relative humidity. Since there was no information on vertical variation of the refractive index,

one value was used here at all altitudes within each layer. Hence, vertical variation of the calculated optical properties within each layer is solely the result of the size distribution variation.

It should be noted that the size distribution retrievals were carried out using a constant refractive index (not dependent on particle size and wavelength), since this is how the inversion code is set up. As shown in Part I, and also discussed by *King et al.* [1978] and *Gonzalez Jorge and Ogren* [1996], this assumption affects the resulting size distributions. This leads to the conclusion that the size distributions retrieved here, combined with the size-resolved refractive index, do not necessarily reproduce the spectral shape of the measured extinction. In order to create an aerosol model consistent with the sunphotometer measurements, the size distribution retrievals were repeated for several different refractive index values, chosen from the range of values at different particle sizes. In this way, the size distribution result which, along with the size resolved refractive index, reproduces well the measured spectral dependence of the extinction, was found.

For the calculation of aerosol optical properties, Mishchenko's Mie code [*Mishchenko et al.*, 1999; *De Rooij and Van der Stap*, 1984] was employed in the case of the boundary and pollution layers. The assumption of spherical particles in the dust layer however, may lead to erroneous results when the optical properties are calculated, since the dust particles are of irregular shapes [*Sokolik et al.*, 2001; *Kalashnikova and Sokolik*, 2002, 2004]. Studies that investigated the effect of this assumption on various calculated aerosol properties [*Mishchenko et al.*, 1997; *Pilinis and Li*, 1998] show that, while the optical thickness and single scattering albedo are not significantly affected by the particle nonsphericity, the backscattering phase function at 180° is overestimated by use of Mie theory in the case of nonspherical particles. Therefore, the calculation of the lidar ratio profile in the dust layer was carried out under the assumption of nonspherical particles, using a model of surface-equivalent randomly oriented

oblate spheroids. For this purpose, the T-matrix algorithm [*Mishchenko and Travis*, 1998] was employed. The degree of particle nonsphericity is defined by the aspect ratio (the ratio of largest to smallest particle dimension). As these calculations are very CPU intensive, only one particle shape, defined by the aspect ratio 1.9, was considered here.

3.2. Lidar ratio predicted by the two size distribution profiles

Vertically resolved lidar ratios modeled using the measured and retrieved size distributions (Figure 1) exhibit differences in the boundary and pollution layers, due to differences between the corresponding backscattering phase functions. In the dust layer however, similar lidar ratio results for the two size distribution profiles were found. Note that the discontinuities in the modeled lidar ratio profile at the boundaries between the layers are a result of the change of refractive index used in the calculations.

Both size distribution models yield similar single scattering albedo values, with not much vertical variability within each layer, as a result of its stronger dependence on the refractive index than its dependence on the particle size. The chemical composition analysis implied non-absorbing particles in the boundary layer [*Wang et al.*, 2002], which resulted in the single scattering albedo values equal to 1.0. Single scattering albedo values of 0.78 – 0.81 in the pollution layer, and 0.93 – 0.96 in the dust layer, were found from both size distribution profiles. Particles in these two layers were absorbing due to the presence of elemental carbon in the accumulation mode, and dust in the coarse mode respectively [*Wang et al.*, 2002]. Comparison of the single scattering albedo values in the dust layer with those obtained using Mie theory (not shown here) confirm that this aerosol property is largely unaffected by particle nonsphericity. *Mishchenko et al.* [1997] found that the effect on the single scattering albedo is small if the particle effective size parameter (defined as $2\pi r_{eff}/\lambda$, where r_{eff} is the particle

effective radius, and λ is the wavelength) is larger than about 1.0; in the case studied here the effective size parameter is ~10-15 for the retrieved, and ~ 8 for the measured size distributions.

The lidar ratio profile that results from the retrieved size distribution shows little variability in the pollution and dust layers (34.4 *sr* – 43.3 *sr* and 27.4 *sr* – 33.5 *sr* respectively), and an increase with altitude in the boundary layer (10.4 *sr* – 21.8 *sr*). This increase in the boundary layer is a result of an increase in the relative contribution of the small particle mode to the total concentration, suggested by stronger wavelength dependence of aerosol extinction as altitude increases in the boundary layer (left panel of Figure 1), and revealed by comparison of the retrieved size distributions at different altitudes (not shown here). *Liu et al.* [2002] also noted that an increase in the relative contribution of small particles results in an increased lidar ratio. Except for the dust layer, the lidar ratio calculated from the measured size distributions exhibit more vertical variability and generally larger values than those resulting from the retrieved size distributions.

Since the same refractive index values were used in both models for calculation of the lidar ratio profile, it is useful to compare the retrieved and measured size distributions at different altitudes in order to explain the differences between the corresponding lidar ratios. The retrieved size distributions at altitudes close to the altitudes of the in-situ measurements were selected for comparisons. For better understanding of the effect of the differences in these size distributions on the computed lidar ratio values, the relative contributions of particles in different size ranges to extinction and backscattering coefficients were calculated following *Russell et al.* [1981] and *Reagan et al.* [1988]:

$$R_{ext,bk}(\bar{r}) = \frac{\int_{r_1}^{r_2} \pi r^2 Q_{ext,bk}(r,\lambda,m)dr}{\int_{r_1}^{r_2} \pi r^2 Q_{ext,bk}(r,\lambda,m)dr}. \qquad (3)$$

$R_{ext,bsc}(\tilde{r})$ is the relative contribution of the particles with radii smaller than $\tilde{r}$, to the extinction or backscattering due to all particles between lower and upper radius limits (r_1 and r_2) of the given size distribution. The relative contributions calculated at λ = 0.523 μm for selected size distributions (in-situ measured and retrieved from extinction spectrum at altitude close to that of in-situ measurements) are shown in Figures 2 and 3.

Examining the differences between the retrieved and measured size distributions, in parallel with the corresponding contribution factors, reveals the following major reason for the generally smaller lidar ratio predicted by the retrieved size distributions. Compared to the measured size distributions, the retrieved distributions have larger concentrations at both small and large particle ends in comparison with the measured size distributions. The contribution of these particles to the backscattering coefficient is generally larger than their contribution to extinction, particularly at the large particle end, leading to a smaller lidar ratio. An example is shown in Figure 2, where there is a large difference between the modeled lidar ratios (40.4 *sr* and 50.1 *sr* for retrieved and measured size distribution, respectively), mainly due to overestimated concentration at large particle end by the retrieval algorithm. A typical example of comparison of retrieved and measured size distributions in the dust layer is shown in the Figure 3. Here, the coarse mode is a significant contributor to both extinction and backscattering coefficients, and the differences in these coefficients resulting from the two size distributions largely cancel out when calculating the lidar ratio.

3.3. Comparison of the modeled lidar ratio with the measurements

The vertically resolved lidar ratio implied by the extinction profile [*Schmid et al.*, 2003] is also shown in Figure 1, for comparison with the modeled values. The implied lidar ratio has large values in the boundary layer (larger than 50 *sr* in a significant part of the layer), whereas

the modeled values in this layer are close to the lidar ratios of maritime aerosol reported in the literature. A modeling study by *Ackermann* [1998] resulted in a lidar ratio of ~15-30 *sr* at 0.532 μm for a range of relative humidities. *Masonis et al.* [2003] reported a value of 25.4 ± 3.5 *sr* at the same wavelength, obtained from measurements using an integrating nephelometer, Particle Soot Absorption Photometer (PSAP), and a 180°-backscatter nephelometer, under clean marine conditions, for near-ambient relative humidity. Using MPL/sunphotometer measurements during the INDOEX campaign, *Welton et al.* [2002] obtained a value of 33 ± 6 *sr* for the marine aerosols without continental influence.

In the dust layer, modeled lidar ratio is in the range between 27.4 *sr* and 33.5 *sr*, generally lower than the implied lidar ratio, and also lower than the directly measured lidar ratio values for Asian dust reported in other studies. *Sakai et al.* [2002] reported an average lidar ratio value of 46 ± 5 *sr* obtained by Raman lidar measurements at 0.532 μm, for an elevated dust layer over Tsukuba, on April 23. Studying Asian dust events in 1998 and 1999, using a high-spectral-resolution lidar and a combined Raman elastic-backscatter lidar, *Liu et al.* [2002] reported height-averaged values of 42 *sr* – 55 *sr* at two sites in Japan. A possible reason for low lidar ratio values obtained in the present study is the use of a simple model of a single shape of the aerosols. Asian dust aerosols exhibit a wide distribution of aspect ratio values [*Okada et al.*, 1987], and therefore the assumption of a single shape is expected to affect the modeled backscattering phase function [*Mishchenko et al.*, 1997]. Calculation of the lidar ratio, carried out by *Liu et al.* [2002] using size distributions retrieved from Sun/sky radiometer measurements at two sites in Japan, resulted in significantly larger values assuming a model of randomly oriented prolate spheroids, compared to results for oblate spheroids with the same aspect ratio (the largest difference was 43%). Furthermore, *Kalashnikova and Sokolik* [2002; 2004] showed that the scattering phase function of sharp-edge particles, identified in

SEM/TEM images of dust samples, differ from those obtained with a smooth particle shape model, such as the spheroidal model.

In the pollution layer, the lidar ratio values calculated from the retrieved size distributions are closer to the implied values than those calculated from the measured particle size distributions. The differences between the lidar ratios resulting from the retrieved size distributions, and the implied lidar ratios at different altitudes in this layer, range from 7% to 46%. Since the modeled lidar ratio values depend on the accuracy of the estimate of aerosol size distribution and refractive index, we examine the effect of changes of these properties (in this layer), in order to understand the differences between the results of the model and the measurements.

The size distributions retrieved from the spectral dependence of aerosol optical properties are not unique [*King et al.*, 1978; *King et al.*, 1982]. Furthermore, the constrained linear inversion method yields the size distribution only in the limited particle size range in which the particles contribute significantly to the extinction measurements. Lack of information beyond the radius limits of the retrieval can cause uncertainties in the modeled backscattering. In addition, these size distributions tend to overestimate particle concentration at the ends of the radius interval of retrieval, as noted earlier. Therefore, an attempt was made here to find the bimodal lognormal size distributions equivalent to those retrieved using the constrained linear inversion method (in the sense that they reproduce the measured extinction spectra), which are also in agreement with the implied lidar ratio values. For this purpose, the look-up-table (LUT) approach was used. In order to generate the look-up-table, the aerosol optical properties (extinction and scattering coefficients, and phase function in the backward direction) were calculated for a range of lognormal functions, using the same size-resolved refractive index which was used in the previous calculations.

The bimodal lognormal size distribution function is defined as:

$$n(r) = \sum_{i=1}^{2} \frac{N_{0i}}{\sqrt{2\pi}\sigma_i} \exp\left(-\frac{(\ln r - \ln r_{mi})^2}{2\sigma^2}\right), \quad (4)$$

where N_{0i} is the total particle concentration, and r_{mi} and σ_i are the mode radius and width of the i-th mode. Modal radius of the accumulation mode was varied between 0.04 μm and 0.20 μm, with the step of 0.02 μm, while the modal radii of the coarse mode were chosen in the range 0.50-1.30 μm, with increments of 0.05 μm. The respective widths were varied in the range 0.40-0.70 and 0.40-0.90, for the accumulation and coarse mode, with the step of 0.05. While this range of parameters for the accumulation mode is made to include the values resulting from size distribution retrievals using the non-linear least squares method in Part I, in the case of the coarse mode, larger values had to be considered in order to enhance the backscattering coefficient. The fine and coarse lognormal modes were then combined in order to find the size distributions so that the calculated optical properties agree with the sunphotometer measurements and the implied lidar ratio. For all combinations of fine and coarse modes from the look-up-table, the following quantities were calculated:

$$\varepsilon_{ext} = \sqrt{\frac{1}{13}\sum_{i=1}^{13}\left(\frac{\sigma_{ext}^{meas} - \sigma_{ext}^{calc}}{\sigma_{ext}^{meas}}\right)^2}, \quad (5)$$

and

$$\Delta_S = \frac{\left|S^{implied} - S^{calc}\right|}{S^{implied}}. \quad (6)$$

Here, $\sigma_{ext}^{meas}(\lambda)$ and $\sigma_{ext}^{calc}(\lambda)$ are measured and calculated aerosol extinction coefficients at wavelength λ, while $S^{implied}$ and S^{calc} are the implied and calculated lidar ratios.

Requiring that $\varepsilon_{ext} < 0.03$, and $\Delta_S < 0.10$, multiple solutions were obtained. However, in all cases, the solutions were grouped around a single combination of parameter values. The

best solution was found from minimizing the sum of squares of these two residual quantities. These size distributions exhibit wide coarse mode, since the large particles need to be included to increase the backscattering, and consequently decrease the lidar ratio. In addition, these size distributions yield somewhat larger single scattering albedo. Comparison of the resulting lidar ratio vertical profile with the implied one (in the pollution layer) is shown in Figure 4. We also compared the LUT-derived size distributions with those retrieved from the same extinction spectra using the constrained linear inversion method. At all altitudes considered, the smaller lidar ratio produced by the LUT-derived size distributions is achieved by large values of the coarse mode radius and width. This increases the backscattering, but also increases the optical thickness and in some cases leads to deviation in optical thickness at large wavelengths. Two typical cases are shown in Figure 5. Case 1 is for the altitude h = 0.63 *km*, where the largest disagreement between the implied lidar ratio and the one modeled by the retrieved size distribution was obtained, with a relative lidar ratio difference of 46%. The LUT-derived size distribution yields 38% larger backscattering than the size distribution retrieved using the constrained linear inversion method. Figure 5 also shows the extinction spectrum predicted by the LUT-derived size distribution, in comparison with that derived from the sunphotometer measurements. The differences at the two largest wavelengths are still within the estimated uncertainties of the sunphotometer-derived extinction. Case 2 corresponds to the altitude of h = 1.45 *km*. The size distributions obtained by the two methods agree quite well. The LUT-derived mode radius of the coarse mode is smaller than that in Case 1, whereas the width is the same. This results in a smaller increase of backscattering in this case (11%), which is enough to achieve almost exact agreement with the implied lidar ratio at this altitude.

Lack of vertical variability of the particle refractive index in the model used in this work is another possible reason for the lack of greater vertical variability of the modeled lidar ratio and its deviation from the implied lidar ratio. In support of this assumption, a relatively

small relative difference between the lidar ratio calculated from the retrieved size distribution and the implied lidar ratio (10%) was obtained close to the altitude of 1.38 *km*, at which the MOUDI and denuder samples for the pollution layer particle chemical composition analysis were taken [*Wang et al.*, 2002]. Therefore, the effect of a change in the refractive index was tested here by increasing the real part and decreasing the imaginary part by a constant percentage through the entire size range, to decrease the modeled lidar ratio. This analysis suggests that no significant improvement of results could be achieved at the altitudes at which there were large deviations of calculated lidar ratio from the implied one, by increasing the real part of the refractive index without also changing the imaginary part. However, agreement could be obtained by substantially decreasing the imaginary part of the refractive index (up to 70%), resulting in significantly higher single scattering albedo. At the altitudes where the largest difference between the modeled and implied lidar ratio values was obtained (around 45%), the decrease of the imaginary part of refractive index required to obtain the agreement between these lidar ratios resulted in a single scattering albedo value of 0.92. It is noteworthy that the pollution layer single scattering albedo values derived from in-situ measurements, reported in other studies [*Anderson et al.*, 2003; *Markowicz et al.*, 2003; *Carrico et al.*, 2003; *Quinn et al.*, 2004], and Spectral Solar Flux Radiometer (SSFR) measurements [*Bergstrom et al.*, 2003], are also significantly larger than those implied by the model used here, as will be discussed in the Section 4.

4. Aerosol radiative effects

The aerosol effect on climate was estimated by evaluating the radiative forcing and heating rates. The aerosol radiative forcing is defined as the perturbation of the net flux (the difference between the downwelling and upwelling irradiances) at a certain altitude, caused by aerosols:

$$F_{net} = F_{\downarrow} - F_{\uparrow}. \quad (7)$$

$$forcing = F_{net}(with\ aerosol) - F_{net}(without\ aerosol). \quad (7')$$

The local heating effect of aerosol is described by the heating rate, which is defined by:

$$\frac{\partial T}{\partial t} = -\frac{1}{\rho c_p}\frac{\partial F_{net}}{\partial z}, \quad (8)$$

where ρ and c_p are the air density and the specific heat capacity at constant pressure.

In order to estimate the radiative effects of the aerosol profile observed on April 17, 2001, the Fu-Liou radiative transfer code [*Fu and Liou*, 1992; 1993; *Kay et al.*, 2001] was employed. It takes into account Rayleigh scattering, gas absorption, and the radiative effects of aerosols and clouds. The delta-four-stream method was used for solving the radiative transfer equation. The code performs calculation of irradiances in the 0.2 - 40.0 μm wavelength range, which covers the solar and thermal spectral regions. This wavelength interval is divided into 18 bands: 6 in the shortwave (0.2 - 4.0 μm), and 12 in the longwave (4.0 - 40.0 μm) region. The radiative transfer model uses the correlated k-distribution method for band-averaging of rapidly varying gas absorption coefficients. In this work, only direct aerosol radiative effects (under clear sky conditions) in the solar spectral region are considered.

4.1. Input parameters

Aerosol optical properties required as an input to the radiative transfer code are aerosol extinction optical thickness, absorption optical thickness, and the asymmetry parameter. Focusing on the solar spectrum, these have been calculated for each of the three layers of the studied vertical profile, using the size distributions retrieved from the measured layer optical thicknesses. Note that the size-resolved refractive indices determined by *Wang et al.* [2002] on the basis of the aerosol chemical analysis, and used in previous calculations of aerosol optical properties in this paper, are wavelength-independent and representative of the visible part of

the spectrum. Therefore, it is necessary to discuss the effect of its spectral dependence in the wavelength range considered here (0.2 μm – 4.0 μm). Some authors calculated aerosol optical properties for radiative transfer calculations using an assumption of a constant refractive index over a larger wavelength range [*Redemann et al.*, 2000b; *Russell et al.*, 1999]. *Formenti et al.* [2002] used a constant refractive index value to calculate shortwave aerosol forcing and noted that this was a reasonable approximation at wavelengths below 2.5 μm, but may lead to errors above this wavelength.

We used two refractive index models to evaluate aerosol optical properties. In the first model, the refractive index is assumed to be constant, and *Wang et al.*'s [2002] refractive index values are assumed to be representative at the entire solar spectrum. The other model assumes wavelength-dependent refractive index, with *Wang et al.*'s [2002] values representative only of the mid-visible part of the spectrum. In order to extrapolate these values to the remaining part of the spectrum, they were required to follow the wavelength dependence of refractive index estimated on the basis of the information on aerosol chemical composition given by *Wang et al.* [2002], and the wavelength-dependent refractive index values for different aerosol types, provided in the Optical Properties of Aerosols and Clouds (OPAC) database [*Hess et al.*, 1998]. Following *Conant et al.* [2003], who also used refractive indices from the OPAC database to construct an optical model of aerosol from the ACE-Asia region, refractive indices of pure sulfuric acid were chosen for sulfate and ammonium, those of water soluble aerosol type were used for organic carbon, and refractive indices of soot were used for black carbon. Due to different chemical compositions of the fine and coarse aerosol mode [*Wang et al.*, 2002], in the present work the refractive index was assumed to have a different wavelength dependence for small and large particles. The wavelength dependence of refractive index varies with relative humidity, and the OPAC database provides refractive index values at a range of relative humidities. The values used in this work are based on the average relative

humidities for the layers studied, found to be 55%, 63% and 49% in the boundary, pollution and dust layer, respectively. It should be noted that using these refractive index values for wet aerosol is strictly adequate only if the particles are external mixtures of different components, while an assumption of internal mixture was used here. However the effect is not expected to be significant, since these values were used here only to estimate the wavelength dependence of the refractive index, not its absolute value.

Calculation of aerosol optical properties was based on Mie theory; nonsphericity of dust particles was not considered. As discussed earlier, the aerosol optical depth and single scattering albedo are not significantly affected by particle nonsphericity. *Mishchenko et al.* [1997] showed that the effect of particle nonsphericity on the asymmetry parameter is less than 7%. Nonsphericity of dust particles has also been neglected in other studies on their radiative effects [*Liao and Seinfeld,* 1998; *Myhre and Stordal,* 2001; *Haywood et al.,* 2001; *Kinne and Pueschel,* 2001]. The calculated optical properties were spectrally averaged over the wavelength bands of the radiative transfer code (0.2 – 0.7, 0.7 – 1.3, 1.3 – 1.9, 1.9 – 2.5, 2.5 – 3.5, and 3.5 – 4.0 μm), in the following manner:

$$\tau_{ext,abs} = \frac{\int_{\lambda_1}^{\lambda_2} \tau_{ext,abs}(\lambda)\, d\lambda}{\int_{\lambda_1}^{\lambda_2} d\lambda}, \tag{9}$$

$$g = \frac{\int_{\lambda_1}^{\lambda_2} \tau_{scat}(\lambda) g(\lambda)\, d\lambda}{\int_{\lambda_1}^{\lambda_2} \tau_{scat}(\lambda)\, d\lambda}, \tag{9'}$$

where τ_{ext}, τ_{scat} and τ_{abs} are extinction, scattering and absorption optical thicknesses of each layer, g is the asymmetry parameter, and the wavelengths λ_1 and λ_2 define the wavelength band.

The vertical variability of aerosol optical properties was accounted for by scaling the extinction and absorption optical thicknesses at 0.5 μm by the extinction profile at the same

wavelength, derived from the sunphotometer measurements [*Schmid et al.*, 2003]. In this way, the vertical profile of the particle number concentration was obtained. The lidar measurements aboard the R/V Ronald H. Brown showed that the dust layer extended above the highest altitude of the profile flown by the aircraft (3.43 *km*) [*Schmid et al.,* 2003]. The aerosol profile in the present work was extrapolated to an altitude of 4.14 *km* using the lidar-derived extinction profile. This vertical scaling accounts only for the vertical variability of aerosol concentration, while vertical variability of aerosol size distribution was not taken into account. Single scattering albedo and asymmetry parameter were therefore constant within each layer.

Meteorological parameters, such as temperature, pressure and relative humidity profile, were also required as inputs into the code. The vertical profiles of these parameters were measured aboard the Twin Otter aircraft. At the altitudes above the top of the profile, the profiles for midlatitude summer standard atmosphere were adopted. Also, the vertical profile of ozone for midlatitude summer was used.

Aerosol radiative forcing is very sensitive to the reflectance of the underlying surface. A spectrally independent ocean surface albedo was used. The angular dependence of the surface albedo was accounted for using the empirical formula used before by *Redemann et al.* [2000b] (following parameterization by *Taylor et al.* [1996]):

$$A_s = \frac{0.037}{1.1\,\mu_0^{1.4} + 0.15}. \tag{10}$$

This formula gives a range of values between 0.03 and 0.20 for solar zenith angles from 0° to 85°.

4.2. Results

The band-averaged aerosol optical properties (required as an input into the radiative transfer code) resulting from the two refractive index models (with and without spectral

dependence) show negligible difference in the first three spectral bands (wavelengths below 1.9 μm). The differences in optical thickness and asymmetry parameter (band averaged) become somewhat larger at wavelengths above this value, but still below 7%. However, they are more significant for the absorption coefficient in the wavelength band 2.5 - 3.5 μm, resulting in larger differences in the single scattering albedos (above 15%). The significance of these differences for estimating the aerosol direct radiative forcing in the shortwave region was tested by using both aerosol optical models in the radiative transfer code. As noted previously, only shortwave radiative forcing was considered in this work, under the assumption of cloud-free conditions. The irradiances were calculated assuming the solar zenith angle of 42.2°, which was found to be an average value during the measurements in the vertical profile. Since the two aerosol optical models resulted in very close irradiances (the differences were less than 1 Wm^{-2}), only the results for the wavelength-dependent refractive index model are presented here. The vertical profile of the aerosol radiative forcing shown in Figure 6 (the case of the layered profile) was obtained from the vertical profiles of the irradiances calculated for the cases with and without the total aerosol profile; the case of the atmospheric profile with uniform aerosol properties will be discussed later. The radiative forcing at all altitudes is negative, implying a cooling effect of aerosol. The largest forcing occurred in the pollution layer. It is of particular interest to calculate aerosol forcing at the top of the atmosphere (TOA), which describes the influence of aerosols on the planetary radiation budget, and at the surface, which affects the surface heating, evaporation and convection [*Ramanathan et al.*, 2001]. In the case studied here, the instantaneous forcing at the TOA is -37.9 Wm^{-2}, while the surface forcing is larger (more negative) due to aerosol absorption, and had value of -120.5 Wm^{-2}. While the value at TOA is very close to the values obtained by *Redemann et al.* [2000b] for two cases during the TARFOX campaign, the result for the radiative forcing at the surface is a factor of two larger than the values they obtained. The reason for this large value is probably

large absorption in the pollution layer; 85% of the total change of the aerosol radiative forcing in the aerosol profile occurs in the pollution layer. The pollution layer had the largest optical thickness $\tau_{air}(0.50\ \mu m) = 0.31$, and low single scattering albedo, with the value of $\omega_0(0.50\ \mu m) = 0.80$. Coupled with the ocean surface, which has very low reflectance, and with cloud-free conditions, this leads to significant radiative effects.

The calculated aerosol radiative forcing depends strongly on the aerosol optical properties used as an input into the radiative transfer code. Since the size distributions reproduce the layer optical thicknesses derived from the sunphotometer measurements, this property is considered to be accurately known. *Gonzalez Jorge and Ogren* [1996] estimated the effect of errors in the retrieved size distribution, resulting from different assumptions used in the retrievals, on the calculated optical properties. They concluded that the most accurately calculated aerosol optical property was the asymmetry parameter, with the average error under 9%. Taking their results into account, the aerosol absorption coefficient is the only aerosol property which is not known with reasonable accuracy. Comparison of modeled lidar ratio with that obtained from a combination of sunphotometer and lidar measurements, carried out in Section 3, suggests that the single scattering albedo in the pollution layer is larger than that predicted by the model. Moreover, the modeled single scattering albedo (0.80 at 0.50 μm, with weak spectral dependence in the visible wavelength range) is significantly smaller than the in-situ measurements suggest. The average single scattering albedo of the submicron particle mode in the pollution layers, obtained from the in-situ measurements of particle scattering and absorption aboard the NCAR C-130 aircraft during the ACE-Asia campaign, was 0.88 ± 0.03 at 0.55 μm, at RH below 40% [*Anderson et al.*, 2003]. *Bergstrom et al.* [2003] determined wavelength-dependent single scattering albedo which reproduces aerosol layer fractional absorption derived from SSFR measurements aboard the Twin Otter aircraft. For a layer influenced by pollution and dust, observed on April 12, 2001, they reported a single scattering

albedo value of 0.90 ± 0.02 at 0.55 μm, with stronger wavelength dependence than that of the single scattering albedo calculated here for the pollution layer. *Quinn et al.* [2004] obtained single scattering albedo values of 0.90 – 0.94 for polluted regions at 55% RH, from in-situ measurements aboard the R/V Ronald H. Brown during the ACE-Asia. *Markowicz et al.* [2003] reported single scattering albedo values for polluted airmasses, which are lower than 0.90 (but still above 0.86) at 55% RH. *Carrico et al.* [2003] obtained the single scattering albedo as a function of RH; they used the humidograph nephelometer method to determine dependence of aerosol scattering coefficient on RH, and PSAP measurements of absorption coefficient at 55% RH, and assumed that the change of absorption coefficient with RH is negligible. Their results showed that in the polluted regions during the campaign the single scattering albedo increased from 0.91 to 0.96 for an increase in RH from 40% to 85%. They also reported an average single scattering albedo of 0.94 ± 0.03 at ambient RH (0.71% ± 13%). The single scattering albedo for the dust layer in the present work is 0.94 (at λ = 0.50 μm), which is in agreement with airborne and shipborne in-situ measurements for dust cases. These results suggest that it is of interest to investigate the effect of the uncertainty in single scattering albedo of the pollution layer on the estimated radiative forcing. For that purpose, the imaginary part of the size-resolved refractive index (at 0.50 μm) was decreased by 45% over the complete size range, in order to increase the single scattering albedo at 0.50 μm by ~10%, to the value of 0.88. It was then extrapolated at other wavelengths, assuming the same wavelength dependence as that in the previous calculations. Aerosol radiative forcings that resulted from the larger single scattering albedo are -44.94 Wm^{-2} and -103.82 Wm^{-2} at the TOA and the surface, respectively. Comparison with the previous results (for smaller single scattering albedo) shows larger (more negative) forcing at TOA in this case, and smaller (less negative) forcing at surface. It should be noted that in the case of larger single scattering albedo, the optical thickness of the layer was scaled to the same value as in the previous case.

Therefore, less absorption resulted in larger scattering optical thickness of the layer. The difference between the forcings at the TOA and the surface is smaller than in the previous case (of smaller single scattering albedo), due to less absorption in this case.

In addition to radiative forcing, the heating rates were calculated at different altitudes within the total aerosol column sampled. The vertical profiles of the heating rates due to the total aerosol column were calculated as the difference between heating rates in the presence of aerosol profile, and without aerosols. The heating rate profiles, for the cases of more and less absorption in the pollution layer (ω_0 (0.50 μm) = 0.80, and ω_0 (0.50 μm) = 0.88) are shown in Figure 7. The Figure also shows the case of the uniform aerosol properties of particles through the total column, which is discussed in the next subsection. The results show that the presence of absorbing aerosols causes additional heating within the layer. The largest perturbations in heating rates are in the pollution layer, which is the most absorbing layer observed in the studied profile. The heating rates in this layer range from ~0.5 *K/day* to 5.7 *K/day* in the case of smaller single scattering albedo. The maximum value decreases to 3.6 *K/day* if the larger single scattering albedo is considered. These values are high compared to the values obtained for the dust layer, with maximum of 0.9 *K/day*. The diurnally averaged values obtained by *Haywood et al.* [2001] reported diurnally averaged heating rates in the range from 0.5 *K/day* to 1.0 *K/day* for Saharan dust with single scattering albedo of 0.87 at 0.55 μm. Dust in the present study was less absorbing, with the single scattering albedo of 0.95 at 0.55 μm. Note that the heating rates in the boundary layer are negative and very small. There is no absorption in the boundary layer, and the small negative heating rate is due to absorption and scattering by aerosol above this layer, which caused a decrease in the net downwelling irradiance.

Unlike the case studied here, where three layers with different particle properties were considered, some studies on aerosol direct radiative effect are based on the assumption of vertically uniform aerosol properties [*Yu et al.*, 2001], due to lack of vertically resolved

measurements. Therefore, it is useful to investigate the effect of the assumption of vertically uniform particle optical properties. For that purpose, effective aerosol optical properties of the total aerosol column were defined as follows:

$$\tau_{ext,eff} = \sum_i \tau_{ext,i}, \tag{11}$$

$$\tau_{abs,eff} = \sum_i \tau_{abs,i}, \tag{11'}$$

$$g_{eff} = \frac{\sum_i g_i \tau_{sc,i}}{\sum_i \tau_{sc,i}}. \tag{11''}$$

Here, τ_{ext}, τ_{abs}, τ_{sc}, and g are extinction, absorbing and scattering optical thickness, and asymmetry parameter, respectively. The subscript i denotes a layer (boundary, pollution, or dust layer), while the subscript *eff* is used for the effective aerosol optical properties. Using the formulas above, the effective optical properties were calculated for each of the six solar spectral bands of the Fu-Liou code, from the corresponding band averaged properties for the three layers of the profile. These properties were used as an input into the radiative transfer code to calculate the aerosol radiative forcing and the heating rates. The vertical profile of aerosol extinction was the same as in the previous calculations.

The radiative forcing (both at the TOA and at the surface) exhibited very small difference from the previous results (less than 1 Wm^{-2}), suggesting that these properties do not depend on the vertical distribution of single scattering albedo and asymmetry parameter. However, the vertical distribution of radiative forcing and heating rates changed (Figures 6 and 7).

As seen in Figure 7, the heating rates in the boundary and dust layers are larger than in the case of the layered atmosphere, since the single scattering albedo in this case is lower (the average value of 0.86 in the first band) than in the previous calculations (1.0 and 0.94 for the

boundary and dust layers, respectively). For a similar reason, absorption in the pollution layer is slightly decreased.

5. Conclusion

Comparison between the modeled lidar ratio and that derived from collocated airborne sunphotometer and shipborne lidar measurements was carried out for a vertical profile with three distinct aerosol layers, observed during the ACE-Asia campaign. For that purpose, size distributions retrieved from sunphotometer-derived extinction spectra, and those measured in-situ using a combination of DMA and APS flown on the same aircraft as the sunphotometer, were combined with the same size-dependent refractive indices calculated for each layer by *Wang et al.* [2002] on the basis of particle chemical composition analysis. The calculated single scattering albedos did not show significant vertical variability, and the values of 0.78-81 and 0.93-0.96 in the pollution and dust layer, respectively, were obtained from both size distribution profiles. These values are consistent with the in-situ measurements [*Anderson et al.*, 2002; *Markowicz et al.*, 2003; *Carrico et al.*, 2003; *Quinn et al.*, 2004] in the case of the dust layer, whereas our model implies significantly more absorbing aerosol in the pollution layer than predicted by the measurements.

Except for the dust layer, the retrieved size distribution led to generally smaller lidar ratio than that derived from the measured size distributions, mainly due to high concentration at the small and large particle ends of the retrieved distributions. In the boundary layer however, both size distributions yielded values in the range ~10 *sr* – 22 *sr*, in agreement with lidar ratios reported for maritime aerosol in the literature [*Ackerman et al.*, 1998; *Welton et al.*, 2002; *Masonis et al.*, 2003]. Low modeled values in the dust layer, compared to that required to reach exact agreement between the extinction profiles derived from the sunphotometer and the lidar measurements (the 'implied' lidar ratio), calculated by *Schmid et al.* [2003], and also compared to the Asian dust lidar ratio measured directly using Raman lidar and high spectral resolution

lidar [*Sakai et al.*, 2002; *Liu et al.*, 2002], are probably a result of using a single shape nonspherical model in the calculations. In the pollution layer, the retrieved size distributions yielded better agreement with the implied lidar ratio than those measured in-situ, with relative differences ranging from 7% to 46%. These differences most probably result from a combination of non-uniqueness of the retrieved size distributions and lack of information on vertical variability of aerosol refractive index. However, even for the constant refractive index through the layer, we were able to find size distributions (at all altitudes in the pollution layer) which reproduce both the sunphotometer-derived extinction spectra and the lidar/sunphotometer derived lidar ratio (implied lidar ratio), confirming consistency between the sunphotometer and lidar measurements.

Aerosol radiative effects were estimated using aerosol optical model defined by the retrieved size distributions, and refractive index model constructed by adjusting *Wang et al.*'s [2002] values to account for the wavelength dependence. Shortwave aerosol radiative forcing and heating rates have been calculated for solar zenith angle of 42.2°, under the assumption of clear sky conditions. The radiative forcings at the TOA and the surface were -37.9 Wm^{-2} and -120.5 Wm^{-2}, respectively. Very large aerosol radiative forcing at the surface was mainly due to the highly absorbing pollution layer. A 10% increase of the single scattering albedo (from 0.80 to 0.88 at 0.50 μm) led to larger forcing at TOA (-44.9 Wm^{-2}), and smaller at the surface (-103.8 Wm^{-2}). This increase in the single scattering albedo caused a decrease of the heating rates in the layer by a factor of ~1.6. It was shown that information on vertical structure of aerosol single scattering albedo and asymmetry parameter is not significant for estimating radiative forcing at the TOA and the surface if the extinction profile is known. It is however, important in order to accurately estimate the vertical profiles of forcing and heating rates.

Acknowledgements

This work was carried out while one author (M. K.) was supported by an International Postgraduate Research Scholarship, funded by the Australian Department of Education, Science and Training (DEST)

6. References

Ackermann, J., 1998: The extinction-to-backscatter ratio of tropospheric aerosol: A numerical study, *J. Atmos. Oceanic Technol.*, **15,** 1043-1050

Anderson L. T., S. J. Masonis, D. S. Covert, N. C. Ahlquist, S. G. Howell, A. D. Clarke, and C. S. McNaughton, 2003: Variability of aerosol optical properties derived from in situ aircraft measurements during ACE-Asia, *J. Geophys. Res.*, **108 (D23),** 8647, doi:10.1029/2002JD003247

Ansmann, A., M. Riebesell, and C. Weitkamp, 1990: Measurement of atmospheric aerosol extinction profiles with a Raman lidar, *Opt. Lett.*, **15,** 746-748

Ansmann, A., M. Riebesell, U. Wandinger, C. Wietkamp, E. Voss, W. Lahmann, and W. Michealis, 1992: Combined Raman elastic-backscatter lidar for vertical profiling of moisture, aerosol extinction, backscatter, and lidar ratio, *Appl. Phys. B* **55,** 18-28

Ansmann, A., U. Wandinger, A. Wiedensohler, and U. Leiterer, 2002: Lindenberg Aerosol Characterization Experiment 1998 (LACE 98): Overview, *J. Geophys. Res.*, **107 (D21),** 8129, doi:10.1029/2000JD000233

Bane, J. M., Bluth, R., Flagg, C., Jonsson, H., Melville, W. K., Prince, M., Riemer, D. UNOLS now Oversees Research Aircraft Facilities for Ocean Science. *Eos Trans. AGU*, **85(41),** 402, 2004.

Bates T. S., B. J. Huebert, J. L. Gras, F. B. Griffiths, and P. A. Durkee, 1998: International Global Atmospheric Chemistry (IGAC) Project's First Aerosol Characterization Experiment (ACE 1): Overview, *J. Geophys. Res.*, **103 (D13)**, 16,297-16,318

Bergstrom, R. W., P. Pilewskie, J. Pommier, M. Rabbette, P. B. Russell, B. Schmid, J. Redemann, A. Higurashi, T. Nakajima, P. K. Quinn, 2003: Spectral absorption of solarradiation by aerosols during ACE-Asia, *J. Geophys. Res.*, **109**, D19S15, doi:10.1029/2003JD004467

Carrico, C. M., P. Kus, M. J. Rood, P. K. Quinn, and T. S. Bates, 2003: Mixtures of pollution, dust, sea salt, and volcanic aerosol during ACE-Asia: Radiative properties as a function of relative humidity, *J. Geophys. Res.*, **108 (D23)**, 8650, doi:10.1029/2003JD003405

Conant, W. C., J. H. Seinfeld, J. Wang, G. R. Carmichael, Y. Tang, I. Uno, P. J. Flatau, K. M. Markowicz, and P. K. Quinn, 2003: A model for the radiative forcing during ACE-Asia derived from CIRPAS Twin Otter and R/V *Ronald H Brown* data and comparison with observations, *J. Geophys. Res.*, **108 (D23)**, 8661, doi:10.1029/2002JD003260

De Rooij, W. A., and C. C. A. H. Van der Stap, 1984: Expansion of Mie scattering matrices in generalized spherical functions, *Astronomy and Astrophysics*, **131**, 237-248

Ferrare, R. A., S. H. Melfi, D. N. Whiteman, K. D. Evans, M. Poellot, and Y. J. Kaufman, 1998: Raman lidar measurements of aerosol extinction and backscattering 2. Derivation of aerosol real refractive index, single-scattering albedo, and humidification factor using Raman lidar and aircraft size distribution measurements, *J. Geophys. Res.* **103 (D16)**, 19,673-19,689

Fiebig, M., A. Petzold, U. Wandinger, M. Wendisch, C. Kiemle, A. Stifter, M. Ebert, T. Rother, and U. Leiterer, 2002: Optical closure for an aerosol column: Method, accuracy,

and inferable properties applied to a biomass-burning aerosol and its radiative forcing, *J. Geophys. Res.*, **107 (D21)**, 8130, doi:10.1029/2000JD000192

Formenti, P., O. Boucher, T. Reiner, D. Sprung, M. O. Andreae, M. Wendisch, H. Wex, D. Kindred, M. Tzortziou, A. Vasaras, and C. Zerefos, 2002: STAARTE-MED 1998 summer airborne measurements over the Aegean Sea. 2. Aerosol scattering and absorption, and radiative calculations, *J. Geophys. Res.*, **107 (D21)**, 4451, doi:10.1029/2001JD001536

Fu, Q., and K. N. Liou, 1992: On the correlated k-distribution method for radiative transfer in nonhomogeneous atmospheres, *J. Atmos. Sci.*, **49**, 2139-2156

Fu, Q., and K. N. Liou, 1993: Parameterization of the radiative properties of cirrus clouds, *J. Atmos. Sci.*, **50**, 2008-2025

Gonzalez Jorge, H. and J. A. Ogren, 1996: Sensitivity of retrieved aerosol properties to assumptions in the inversion of spectral optical depths, *J. Atmos. Sci.*, **53**, 3669-3683

Haywood, J. M., P. N. Francis, M. G. Glew, and J. P. Taylor, 2001: Optical properties and direct radiative effect of Saharan dust: A case study of two Saharan dust outbreaks using aircraft data, *J. Geophys. Res.*, **106 (D16)**, 18,417-18,430

Hess, M. P. Koepke, and I. Schult, 1998: Optical Properties of Aerosols and Clouds: The Software Package OPAC, *Bull. Am. Meteor. Soc.*, **79**, 831-844

Holben, B. N., et al., 1998: AERONET: A federated Instrument Network and Data Archive for Aerosol Characterization, *Remote Sens. Environ.*, **66**, 1-16

Huebert, B. J., T. Bates, P. B. Russell, G. Shi, Y. J. Kim, K. Kawamura, G. Carmichael, and T. Nakajima (2003), An overview of ACE-Asia: Strategies for quantifying the relationships between Asian aerosols and their climatic impacts, *J. Geophys. Res.*, **108(D23)**, 8633, doi:10.1029/2003JD003550

IPCC, 2001: *Climate Change 2001: The Scientific Basis. Contribution of Working Group I to the Third Assessment Report of the Intergovernmental Panel on Climate Change* [Houghton, J. T., Y. Ding, D. J. Griggs, M. Noguer, P. J. van der Linden, X. Dai, K. Maskell, and C. A. Johnson (eds.)]. Cambridge University Press, Cambridge, United Kingdom and New York, NY, USA, 881pp.

Kalashnikova, O., and I.N. Sokolik, 2002: Importance of shapes and composition of wind-blown dust particles for remote sensing at solar wavelengths. *Geophys. Res. Lett.*, **29,** No.10, 10.1029/2002GL014947

Kalashnikova, O. V. and I. N. Sokolik, 2004: Modeling the radiative properties of nonspherical soil-derived mineral aerosols, *JQSRT*, **87,** 137-166

Kay, M. J., M. A. Box, T. Trautmann, and J. Landgraf, 2001: Actinic flux and net calculations in radiative transfer – A comparative study of computational efficiency, *J. Atmos. Sci.*, **58,** 3752-3761

King, M. D., D. M. Byrne, B. M. Herman, and J. A. Reagan, 1978: Aerosol size distributions obtained by inversion of spectral optical depth measurements, *J. Atmos. Sci.*, **35**, 2153-2167

King, M. D., 1982: Sensitivity of constrained linear inversions to the selection of the Lagarange multiplier, *J. Atmos. Sci.*, **39,** 1356-1369

Kinne, S., and R. Pueschel, 2001: Aerosol radiative forcing for Asian continental outflow, *Atmos. Environ.*, **35,** 5019-5028

Liao, H., and J. H. Seinfeld, 1998: Radiative forcing by mineral dust aerosols: sensitivity to key variables, *J. Geophys. Res.*, **103 (D24),** 31,637-31,645

Liu, Z., N. Sugimoto, and T. Murayama, 2002: Extinction-to-backscatter ratio of Asian dust observed with high-spectral-resolution lidar and Raman lidar, *Appl. Opt.*, **41,** 2760-2767

Markowicz, K. M., P. J. Flatau, P. K. Quinn, C. M. Carrico, M. K. Flatau, A. M. Vogelmann, D. Bates, M. Liu, and M. J. Rood, 2003: Influence of relative humidity on aerosol radiative forcing: An ACE-Asia experiment perspective, *J. Geophys. Res.*, **108 (D23),** 8662, doi:1029/2002JD003066

Masonis, S. J., T. L. Anderson, D. S. Covert, V. Kapustin, A. D. Clarke, S. Howell, and K. moore, 2003: A study of the extinction-to-backscatter ratio of marine aerosol during the Shoreline Environment Aerosol Study, *J. Atmos. Oceanic Technol.*, **20,** 1388-1402

Melfi S. H., 1972: Remote measurements of the atmosphere using Raman scattering, *Appl. Opt.*, **11,** 1605-1610

Mishchenko, M. I., L. D. Travis, R. A. Kahn, and R. A. West, 1997: Modeling phase functions for dustlike tropospheric aerosols using a shape mixture of randomly oriented polydisperse spheroids: *J. Geophys. Res.*, **102,** 16,831-16,847

Mishchenko, M. I. and L. D. Travis, 1998: Capabilities and limitations of a current FORTRAN implementation of the T-matrix method for randomly oriented, rotationally symmetric scatterers, *J. Quant. Spectrosc. Radiat. Transfer*, **60,** 309-324

Mishchenko, M. I., J. M. Dlugach, E. G. Yanovitskij, and N. T. Zakharova, 1999: Bidirectional reflectance of flat, optically thick particulate layers: an efficient radiative transfer solution and applications to snow and soil surfaces, *J. Quant. Spectrosc. Radiat. Transfer*, **63,** 409-432

Myhre, G. and F. Stordal, 2001: Global sensitivity experiments of the radiative forcing due to mineral aerosols, *J. Geophys. Res.*, **106 (D16),** 18,193-18,204

Nenes, A., S. Pandis, and C. Pilinis, 1998: ISORROPIA: A new thermodynamic equilibrium model for multiphase multicomponent inorganic aerosols, *Aquat. Geochem.*, **4,** 123-152

Okada, K., A. Kobayashi, Y. Iwasaka, H. Naruse, T. Tanaka, and O. Nemoto, 1987: Features of individual Asian dust-storm particles collected at Nagoya, Japan, *J. Meteorol. Soc. Jpn.* **65**, 515-521

Pilinis C., and X. Li, 1998: Particle shape and internal inhomogeneity effect on the optical properties of tropospheric aerosols of relevance to climate forcing, *J. Geophys. Res.*, **103**, 3789-3800

Powell, D. M., J. A. Reagan, M. A. Rubio, W. H. Erxleben, and J. D. Spinhirne, 2000: ACE-2 multiple angle micro-pulse lidar observations from Las Galletas, Tenerife, Canary Islands, *Tellus*, **52B**, 652-661

Quinn, P. K., D. J. Coffman, T. S. Bates, E. J. Welton, D. S. Covert, T. L. Miller, J. E. Johnson, S. Maria, L. Russell, R. Arimoto, C. M. Carrico, M. J. Rood, and J. Anderson, 2004: Aerosol optical properties measured on board the *Ronald H. Brown* during ACE-Asia as a function of aerosol chemical composition and source region, *J. Geophys. Res.*, **109, D19S01**, doi:10.1029/2003JD004010

Rajeev, K. and K Parameswaran, 1998: Iterative method for the inversion of multiwavelength lidar signals to determine aerosol size distribution, *Appl. Opt.* **37**, 4690-4700

Ramanathan et al., 2001: Indian Ocean Experiment: An integrated analysis of the climate forcing and effects of the great Indo-Asian haze, *J. Geophys. Res.*, **106 (D22)**, 28,371-28,398

Reagan, J. A., M. V. Apte, A. Ben-David, and B. M. Herman, 1988: Assessment of aerosol extinction to backscatter ratio measurements made at 694.3 nm in Tuscon, Arizona, *Aerosol Science and Technology*, **8**, 215-226

Redemann J., R. P. Turco, R. F. Pueschel, M. A. Fenn, E. V. Browell, and W. B. Grant, 1998: A multi-instrument approach for characterizing the vertical structure of aerosol properties: Case studies in the Pacific basin troposphere, *J. Geophys. Res.*, **103**, 23,287-23,298

Redemann, J., et al., 2000a: Retrieving the vertical structure of the effective aerosol complex index of refraction from a combination of aerosol in situ and remote sensing measurements during TARFOX, *J. Geophys. Res.*, **105 (D8)**, 9949-9970

Redemann, J., R. P. Turco, K. N. Liou, P. V. Hobbs, W. S. Hartley, R. W. Bergstrom, E. V. Browell, and P. B. Russell, 2000b: Case studies of the vertical structure of the direct shortwave aerosol radiative forcing during TARFOX, *J. Geophys. Res.*, **105 (D8)**, 9971-9979

Russell, P. B., T. J. Swissler, M. P. McCormick, W. P. Chu, J. M. Livingston, and T. J. Pepin, 1981: Satellite and correlative measurements of the stratospheric aerosol. I: An optical model for data conversions, *J. Atmos. Sci.*, **38**, 1279-1294

Russell, P. B., P. V. Hobbs, and L. L. Stowe, 1999: Aerosol properties and radiative effects in the United States East Coast haze plume: An overview of the Tropospheric Aerosol Radiative Forcing Observational Experiment (TARFOX), *J. Geophys. Res.*, **104 (D2)**, 2213-2222

Russell, P. B. and J. Heintzenberg, 2000: An overview of the ACE-2 clear sky column closure experiment (CLEARCOLUMN), *Tellus*, **52B**, 463-483

Sakai, T., T. Shibata, Y. Iwasaka, T. Nagai, M. Nakazato, T. Matsumura, A. Ichiki, Y-S Kim, K. Tmura, D. Troshkin, S. Hamdi, 2002: Case study of Rman lidar measurements of Asian dust events in 2000 and 2001 at Nagoya and Tsukuba, Japan, *Atmos. Environ.*, **36**, 5479-5489

Schmid, B., et al., 2003: Column closure studies of lower tropospheric aerosol and water vapor during ACE-Asia using airborne Sun photometer and airborne in situ and ship-based lidar measurements, *J. Geophys. Res.*, **108 (D23)**, 8656, doi:10.1029/2002JD003361

Shipley, S. T., D. H. Tracy, E. W. Eloranta, J. T. Trauger, J. T. Sroga, F. L. Roesler, and J. A. Wienman, 1983: High spectral resolution lidar to measure optical scattering properties of atmospheric aerosols. 1. Theory and instrumentation, *Appl. Opt.*, **22,** 3716-3724

Sokolik I. N., D. M. Winker, G. Bergametti, D. A. Gillette, G. Carmichael, Y. J. Kaufman, L. Gomes, L. Schuetz, and J. E. Penner, 2001: Introduction to special section: Outstanding problems in quantifying the radiative impacts of mineral dust, *J. Geophys. Res.*, **106 (D16)**, 18,015-18,027

Spinhirne, J. D., J. A. Reagan, and B. M. Herman, 1980: Vertical distribution of aerosol extinction cross section and inference of aerosol imaginary index in the troposphere by lidar technique, *J. Appl. Meteorol.* **19,** 426-438

Spinhirne, J. D., J. A. R. Rall, and V. S. Scott, 1995: Compact eye safe lidar systems, *Rev. Laser. Eng.*, **23,** 112-118

Taylor, J. P., J. M. Edwards, M. D. Glew, P. Hignett, and A. Slingo, 1996: Studies with a flexible new radiation code, II. Comparisons with aircraft short-wave observations, *Q. J. R. Meteorol. Soc.*, **122,** 839-861

Welton, E. J., K. J. Voss, H. R. Gordon, H. Maring, A. Smirnov, B. Holben, B. Schmid, J. M. Livingston, P. B. Russell, P. A. Durkee, P. Formenti, M. O. Andreae, 2000: Ground-based lidar measurements of aerosols during ACE-2: instrument description, results, and comparisons with other ground-based and airborne measurements, *Tellus,* **52B,** 636-651

Welton, E. J., J. R. Campbell, J. D. Spinhirne, and V. S. Scott, 2001: Global monitoring of clouds and aerosols using a network of micro-pulse lidar systems, in *Lidar Remote Sensing for Industry and Environmental Monitoring*, edited by U. N.

Welton, E. J., K. J. Voss, P. K. Quinn, P. J. Flatau, K. Markowicz, J. R. Campbell, J. D. Spinhirne, H. R. Gordon, and J. E. Johnson, 2002: Measurements of aerosol vertical profiles and optical properties during INDOEX 1999 using micropulse lidars, *J. Geophys. Res.*, **107 (D19),** 8019, doi:10.1029/2000JD000038

Wang, J., et al., 2002: Clear-column radiative closure during ACE-Asia: Comparison of multiwavelength extinction derived from particle size and composition with results from Sun photometry, *J. Geophys. Res.*, **107 (D23)**, 4688, doi:10.1029/2002JD002465

Yu, S., C. S. Zender, and V. K. Saxena, 2001: Direct radiative forcing and atmospheric absorption by boundary layer aerosols in the southeastern US: model estimates on the basis of new observations, *Atmos. Environ.*, **35,** 3967-3977

Figure captions

Figure 1. (left) Vertical profile of aerosol extinction at different wavelengths, derived from sunphotometer measurements on April 17 [*Schmid et al.*, 2003]. **(right)** Vertical profiles of the lidar ratio derived from sunphotometer/lidar measurements (implied lidar ratio) [*Schmid et al.*, 2003], and the lidar ratios calculated from the retrieved and in-situ measured size distributions.

Figure 2. (top) Comparison of size distribution retrieved from the sunphotometer-derived extinction spectrum at the altitude of 1.62 *km*, with the in-situ measured distribution at the altitude of 1.64 *km*. **(bottom)** Corresponding extinction and backscattering contribution functions R.

Figure 3. **(top)** Comparison of size distribution retrieved from the sunphotometer-derived extinction spectrum at the altitude of 2.93 *km*, with the in-situ measured distribution at the same altitude. **(bottom)** Corresponding extinction and backscattering contribution functions.

Figure 4. Comparison of lidar ratio calculated from the LUT-derived size distributions with the implied lidar ratio in the pollution layer of the April 17 profile.

Figure 5. Comparison of size distributions, derived using LUT and constrained linear inversion methods from the sunphotometer-derived extinction and corresponding extinction spectra at the altitudes: **(a)** h = 0.63 *km*, and **(b)** h = 1.45 *km*.

Figure 6. Vertical profile of instantaneous aerosol radiative forcing for two scenarios: layered aerosol profile (dotted lines mark boundaries between different layers: marine boundary layer (BL), pollution layer (PL), and free troposphere (FT)); and profile with uniform aerosol single scattering albedo ω_0 and asymmetry parameter g, while the vertical profile of aerosol extinction is the same as in the layered case.

Figure 7. Aerosol heating rates for three scenarios: three aerosol layers, with smaller (0.80 at 0.50 μm) and larger (0.88 at 0.50 μm) single scattering albedo for pollution layer (PL); profile with uniform aerosol single scattering albedo ω_0 and asymmetry parameter g, while the vertical profile of aerosol extinction is the same as in the layered case.

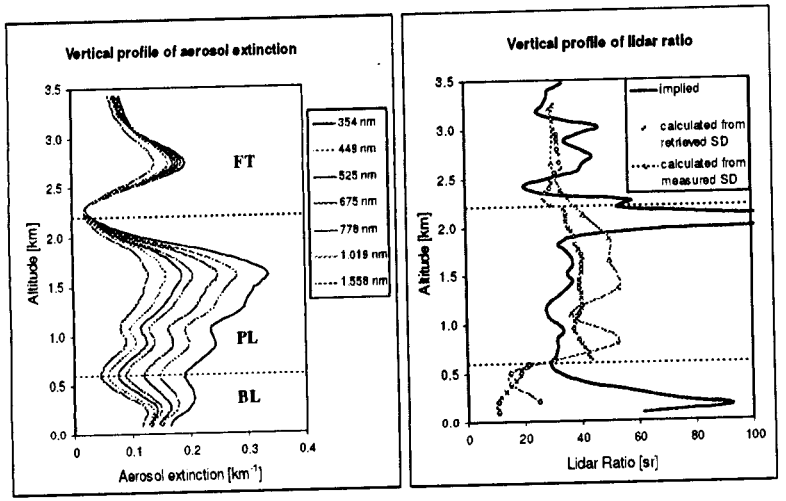

Figure 1. (left) Vertical profile of aerosol extinction at different wavelengths, derived from sunphotometer measurements on April 17 [*Schmid et al.*, 2003]. **(right)** Vertical profiles of the lidar ratio derived from sunphotometer/lidar measurements (implied lidar ratio) [*Schmid et al.*, 2003], and the lidar ratios calculated from the retrieved and in-situ measured size distributions.

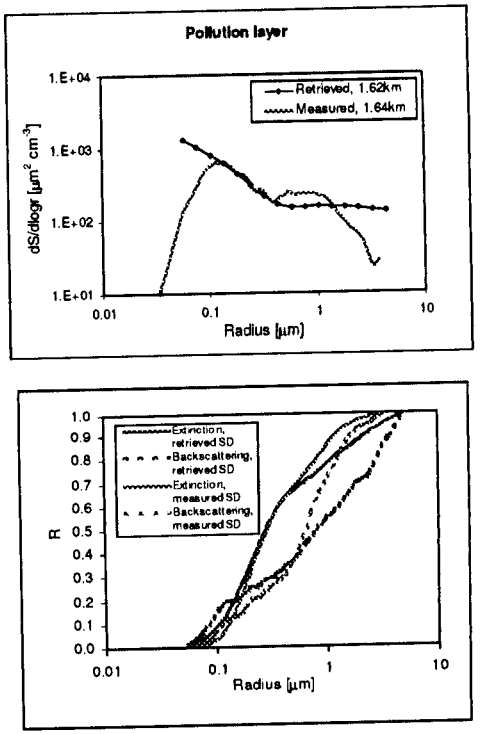

Figure 2. (top) Comparison of size distribution retrieved from the sunphotometer-derived extinction spectrum at the altitude of 1.62 *km*, with the in-situ measured distribution at the altitude of 1.64 *km*. **(bottom)** Corresponding extinction and backscattering contribution functions R.

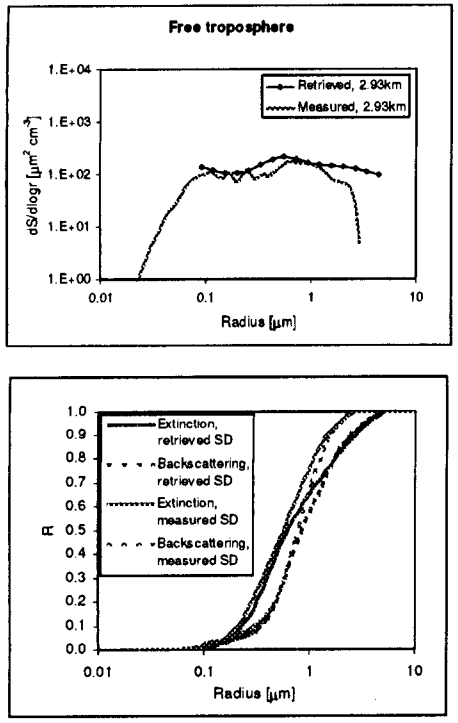

Figure 3. (top) Comparison of size distribution retrieved from the sunphotometer-derived extinction spectrum at the altitude of 2.93 *km*, with the in-situ measured distribution at the same altitude. **(bottom)** Corresponding extinction and backscattering contribution functions.

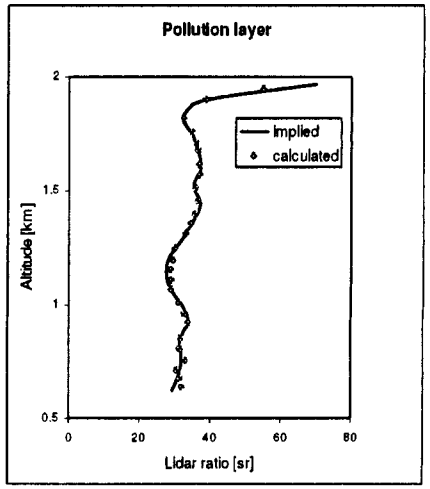

Figure 4. Comparison of lidar ratio calculated from the LUT-derived size distributions with the implied lidar ratio in the pollution layer of the April 17 profile.

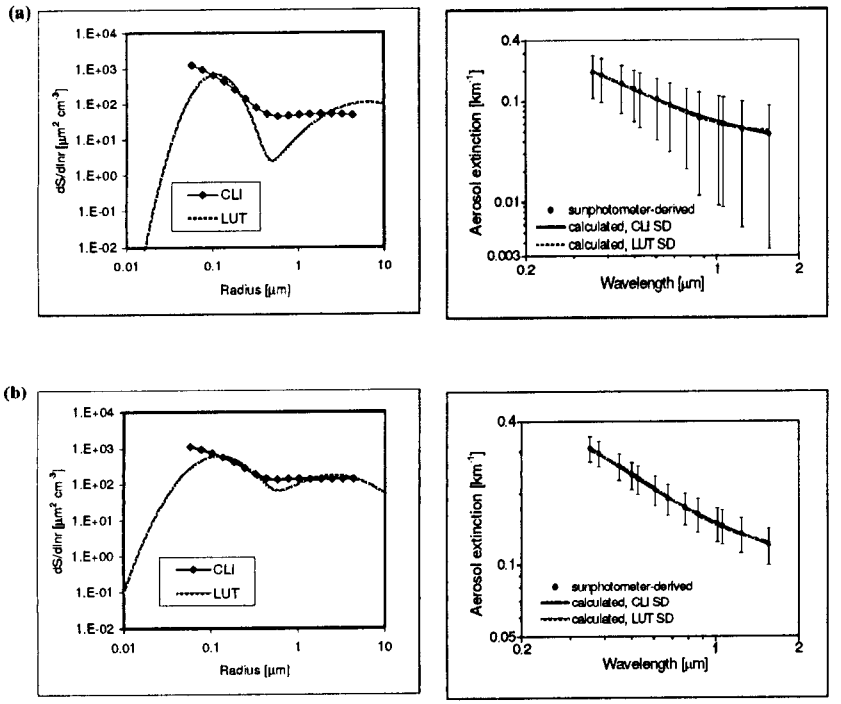

Figure 5. Comparison of size distributions, derived using LUT and constrained linear inversion methods from the sunphotometer-derived extinction and corresponding extinction spectra at the altitudes: **(a)** $h = 0.63$ *km*, and **(b)** $h = 1.45$ *km*.

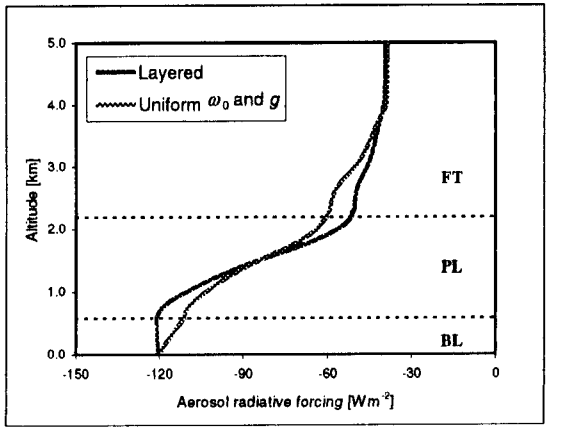

Figure 6. Vertical profile of instantaneous aerosol radiative forcing for two scenarios: layered aerosol profile (dotted lines mark boundaries between different layers: marine boundary layer (BL), pollution layer (PL), and free troposphere (FT)); and profile with uniform aerosol single scattering albedo ω_0 and asymmetry parameter g, while the vertical profile of aerosol extinction is the same as in the layered case.

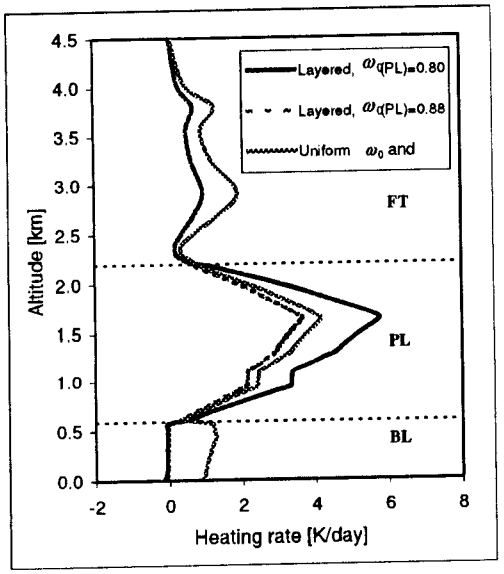

Figure 7. Aerosol heating rates for three scenarios: three aerosol layers, with smaller (0.80 at 0.50 μm) and larger (0.88 at 0.50 μm) single scattering albedo for pollution layer (PL); profile with uniform aerosol single scattering albedo ω_0 and asymmetry parameter g, while the vertical profile of aerosol extinction is the same as in the layered case.